Single cell-resolved study of advanced murine MASH reveals a homeostatic pericyte signaling module

Bendixen, Sofie M.; Jakobsgaard, Peter R.; Hansen, Daniel; Hejn, Kamilla H.; Terkelsen, Mike K.; Bjerre, Frederik A.; Thulesen, Annemette P.; Eriksen, Niels G.; Hallenborg, Philip; Geng, Yana

Published in:
Journal of Hepatology

DOI:
10.1016/j.jhep.2023.11.001

Publication date:
2024

Research Article
Experimental and Translational Hepatology

JOURNAL
OF HEPATOLOGY

Single cell-resolved study of advanced murine MASH reveals a homeostatic pericyte signaling module

Authors

Sofie M. Bendixen, Peter R. Jakobsgaard, Daniel Hansen, …, Aleksander Krag, Blagoy Blagoev, Kim Ravnskjaer

Correspondence

ravnskjaer@bmb.sdu.dk (K. Ravnskjaer).

Graphical abstract

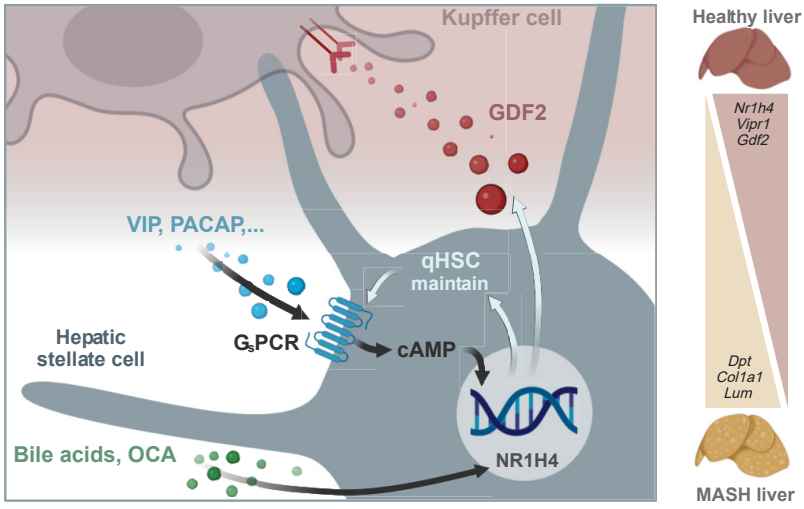

Highlights

- NR1H4/FXR is highly expressed in stellate cells of human and murine livers.
- NR1H4 binding motifs are highly enriched in stellate cell accessible chromatin.
- The NR1H4 agonist obeticholic acid upholds expression of stellate cell identity genes.
- Stellate cell-confined expression of G_SPCR VIPR1 is attenuated in MASH livers.
- cAMP induces stellate cell expression of homeostatic factor GDF2 *in vitro* and *in vivo.*

Impact and implications

Homeostatic interactions between hepatic cell types and their deterioration in metabolic dysfunction-associated steatohepatitis are poorly characterized. In our current single cell-resolved study of advanced murine metabolic dysfunction-associated steatohepatitis, we identified a quiescence-associated hepatic stellate cell-signaling module with potential to preserve normal sinusoid function. As expression levels of its constituents are conserved in the human liver, stimulation of the identified signaling module is a promising therapeutic strategy to restore sinusoid function in chronic liver disease.

https://doi.org/10.1016/j.jhep.2023.11.001
 J. Hepatol. 2024, 80, 467–481

Research Article
Experimental and Translational Hepatology

JOURNAL
OF HEPATOLOGY

Single cell-resolved study of advanced murine MASH reveals a homeostatic pericyte signaling module

Sofie M. Bendixen[1,12,†], **Peter R. Jakobsgaard**[1,12,†], **Daniel Hansen**[1,12,†], **Kamilla H. Hejn**[1,12,†], Mike K. Terkelsen[1,12], Frederik A. Bjerre[1,12], Annemette P. Thulesen[1,12], Niels G. Eriksen[1,12], Philip Hallenborg[1,12], Yana Geng[2], Trine V. Dam[1,12], Frederik T. Larsen[1,12], Charlotte W. Wernberg[3,4,12], Janusa Vijayathurai[1,12], Emma A.H. Scott[1,12], Ann-Britt Marcher[1,12], Sönke Detlefsen[5,11], Lars Grøntved[1,12], Henrik Dimke[6,7], Rebecca Berdeaux[8], Thomas Q. de Aguiar Vallim[9,10], Peter Olinga[2], Mette M. Lauridsen[4,12], Aleksander Krag[3,11,12], Blagoy Blagoev[1,12], Kim Ravnskjaer[1,12,*]

Journal of Hepatology **2024**. vol. 80 | 467–481

Background & Aims: Metabolic dysfunction-associated steatohepatitis (MASH) is linked to insulin resistance and type 2 diabetes and marked by hepatic inflammation, microvascular dysfunction, and fibrosis, impairing liver function and aggravating metabolic derangements. The liver homeostatic interactions disrupted in MASH are still poorly understood. We aimed to elucidate the plasticity and changing interactions of non-parenchymal cells associated with advanced MASH.
Methods: We characterized a diet-induced mouse model of advanced MASH at single-cell resolution and validated findings by assaying chromatin accessibility, bioimaging murine and human livers, and via functional experiments *in vivo* and *in vitro*.
Results: The fibrogenic activation of hepatic stellate cells (HSCs) led to deterioration of a signaling module consisting of the bile acid receptor NR1H4/FXR and HSC-specific G_S-protein-coupled receptors (G_SPCRs) capable of preserving stellate cell quiescence. Accompanying HSC activation, we further observed the attenuation of HSC *Gdf2* expression, and a MASH-associated expansion of a CD207-positive macrophage population likely derived from both incoming monocytes and Kupffer cells.
Conclusion: We conclude that HSC-expressed NR1H4 and G_SPCRs of the healthy liver integrate postprandial cues, which sustain HSC quiescence and, through paracrine signals, overall sinusoidal health. Hence HSC activation in MASH not only drives fibrogenesis but may desensitize the hepatic sinusoid to liver homeostatic signals.

Introduction

Metabolic dysfunction-associated steatohepatitis (MASH) is the result of years of cycling between insults and inadequate regeneration and presents itself as a state of elevated cellular turnover and net deposition of extracellular matrix (ECM). Function of the MASH liver is compromised by inflammation, microvascular dysfunction, and fibrosis, aggravating the initial metabolic derangements. This deterioration of liver function is attributed to hepatocellular plasticity and shifts in cellular communication. Yet, the progression of MASH is incompletely understood, as studies resolving liver plasticity in advanced MASH are scarce. Comprehensive analysis of human MASH is hindered by the sparsity of patient liver biopsies and by patient differences. Single cell-resolved studies of murine liver fibrosis have provided important insights into early disease development[1–3] but only partially recapitulated established human MASH. A thorough account of hepatocellular dynamics in advanced MASH in the face of prolonged dietary challenge is hence needed to delineate the altered cellular fluxes and information circuits amenable to therapeutic intervention.

Herein, we document the phenotypic redefinition of hepatic cell populations in established MASH in mice fed a Western diet for 52 weeks. We lay out the concept that postprandial cues preserve hepatic stellate cell quiescence and sinusoidal homeostasis, which may guide pharmacological intervention in MASH.

Materials and methods

Animal experiments

MASH was introduced in C57BL/6JBomTac mice by Western diet supplemented with D-fructose (42 g/L) in drinking water for 52 weeks. Age-matched control mice were fed standard chow and pure drinking water. Mice were fasted overnight before sacrifice. The *FLEx-TRAP* knock-in mouse was generated from

Keywords: Metabolic dysfunction-associated Steatohepatitis; Hepatic Stellate Cells; Cyclic AMP; G-Protein-Coupled Receptors; ScRNAseq; Inflammation; Sinusoids; Pericytes; Bile Acids; Nuclear Receptors; Transcriptome.
Received 10 December 2022; received in revised form 6 October 2023; accepted 7 November 2023; available online 14 November 2023
Authors names in bold designate shared co-first authorship
* Corresponding author. Address: Dept. of Biochemistry and Molecular Biology, University of Southern Denmark, Campusvej 55, 5230 Odense M, Denmark. Tel.: +4593979317.
E-mail address: ravnskjaer@bmb.sdu.dk (K. Ravnskjaer).
† Equal contribution as first authors.
https://doi.org/10.1016/j.jhep.2023.11.001

the fusion gene *mCherry-Rpl10a*-(IRES)-*FLPo* and the Flip-excision (FLEx)-switch.[4] Gt(ROSA)26Sor$^{tm1(CAG-Chrm3*/GFP,cAMPRE-luc)Berd}$ (G_SD), Tg(Lrat-cre)1Rshw mice (Lrat-cre) were previously described.[5,6] From 12 weeks of age, G_SD and Lrat-cre:G_SD mice were fed the GAN (Gubra-Amylin MASH) diet for 12 weeks. From 2 days before sacrifice, mice were fasted from zeitgeber time 6 to 12 and given 0.1 mg/kg deschloroclozapine in corn oil by oral gavage. On the third day, mice were sacrificed at zeitgeber time 13.5. All animal experiments were approved by the Danish Animal Experiments Inspectorate (approval #2020-15-0201-00603) and adhered to the ARRIVE guidelines.

Immunohistochemistry and staining of FFPE tissues

Mouse liver lobules were immersion-fixed in 4% paraformaldehyde for 16 h and embedded in paraffin (FFPE). For immunohistochemistry (IHC), sections were probed with indicated antibodies (see supplementary methods and table S2) and incubated with EnVision-HRP-coupled anti-rabbit IgG and AEC+ substrate-chromogen solution. Sections were counter-stained with hematoxylin. Human liver biopsies were performed in patients with severe obesity as part of the PROMETHEUS study (ethics approval S-20160006G) conducted in accordance with the guidelines of the Declaration of Helsinki and the principles of good clinical practice. All subjects gave written informed consent for study participation and a separate biobank consent. Human FFPE liver tissue was stained as described previously with minor modifications.[7] Dual PDGFR and NR1H4 IHC immunoreactivity was visualized using DAB+ and Vector SG chromogens. No counter-staining was performed.

Immunofluorescence and single-molecule fluorescence *in situ* hybridization

Fixed-frozen OCT (optimal cutting temperature) compound-embedded liver tissue was cut, permeabilized, and blocked before probing with antibodies and DAPI. Single-molecule fluorescence *in situ* hybridization (FISH) was conducted on FFPE sections using the RNAscope Multiplex Fluorescent Reagent Kit v2 assay according to the manufacturer's instructions. Slides were mounted with ProLong Diamond Antifade Mountant and DAPI and scanned on a Nikon A1 confocal microscope. Images were passed through the AFid algorithm for autofluorescence mitigation. The same settings were used for all images. Single-molecule FISH image quantification was performed using QuPath (v.0.2.3). Digital cell detection was based on DAPI staining. Data visualization and statistics were performed in R.

Whole liver/bulk RNA purification, sequencing, and analysis

Whole liver RNA was extracted by phenol/chloroform and column purification. Libraries were constructed using the NEBNext Ultra RNA Library Prep Kit for Illumina and paired-end sequenced on the NovaSeq 6000. *STAR* was used for alignment of reads to the mm10 genome. *DESeq2* was used to identify differentially expressed genes. Data visualization and statistics were performed in R. A weighted correlation network analysis (WGCNA) was performed using the *WGCNA* R-package based on 5,000 genes with top loadings across the first four principal components.

Gene expression analysis of *Nr1h4* knockout livers

Nr1h4 knockout animals treated with GSK2324 or vehicle for 3 days, whole liver RNA extraction, cDNA synthesis and qPCR analysis were described previously.[8] Relative expression values for all genes of interest were normalized to *Rplp0* (36B4) expression. Differential expression between conditions (false discovery rate <0.05) was determined by pairwise Wilcoxon Rank Sum tests, Benjamini-Hochberg-adjusted for multiple testing. Primer sequences are provided in Table S1.

Whole liver protein purification and mass spectrometry analysis

For quantitative comparison of the liver proteomes, we prepared peptides essentially as described elsewhere.[9] Equal fractions of peptides from all animals were used to generate a spectral library for liquid chromatography mass spectrometry analysis on a Q Exactive HF-X mass spectrometer and data-independent acquisition. Only proteins identified in ≥3 animals per group were included in the analyses. Differentially expressed proteins were identified using DESeq2. Data analysis and visualizations were performed in R.

Hepatic cell isolation for single-cell sequencing and culture

For single-cell RNA sequencing experiments, retrograde liver perfusion was performed as described.[7] Anti-ASGR1 and anti-CD31-conjugated antibodies were used for partial immunodepletion and SYTOX Red for dead cell labeling. From each liver, 20,000 live singlets were sorted and loaded onto the 10x Genomics Chromium controller, and Single-Cell 3' v3 libraries were prepared according to the manufacturer's instructions. For stellate cell culture, cells were separated by density centrifugation and sorted by retinoid content and viability and seeded in 24-well plates with 50,000 cells per well.

Single-cell RNA sequencing data analysis

Sequencing data was demultiplexed, aligned against the mm10 reference genome, quantified, and aggregated using the standardized pipeline in the *Cell Ranger* Single-Cell Software Suite. The *Seurat* package was used for data pre-processing, and doublets removed with *DoubletFinder*. Corrected counts were integrated by *Seurat* batch-correction. For clustering, we used the Seurat implementation of the Leiden algorithm. Testing of differential abundance of subpopulations was performed using *miloR*. Identification of transcription factors and putative target genes was performed in pySCENIC. Mononuclear phagocyte transitions were found using *scVelo*. For diffusion maps, trajectory estimations and differential expression, we used *Destiny* in the R-package *Scater*, *Slingshot*, and *tradeSeq*, respectively. For prediction of ligand-receptor interactions we employed *NicheNet*. Human liver single-nuclei data (GSE212837) were processed with *Seurat*. *DecontX* was used for removal of ambient RNA and *DoubletFinder* for doublet removal. Batch integration was performed in Harmony.

Hepatic stellate cells *in vitro* treatments

All treatments started at 40 h post isolation. Obeticholic acid (OCA): hepatic stellate cells (HSCs) were treated with 10 μM OCA or DMSO for 6 h before harvest. Forskolin: HSCs were treated

with 5 μM forskolin or DMSO for 3 h. For acute effects, cells were harvested immediately. For long-term effects, medium was changed, and HSCs were cultured for an additional 21 h before harvest. OCA/vasoactive intestinal peptide (VIP): HSCs were treated with 5 μM OCA or DMSO for 3 h followed by the addition of 0.5 μM VIP for an additional 3 h before harvest. Cells were harvested in TRIzol, and RNA purified as described above.

ATACseq and single-nucleus ATACseq

Nuclei were isolated from Lrat-cre:*FLEx-TRAP* mouse livers after heart perfusion with 4% PFA followed by dounce homogenization, straining, density centrifugation, and fluorescence-sorting based on DAPI and mCherry (Fig. S5A). Chromatin was tagmented and reverse-crosslinked before column cleanup, PCR amplification, library generation and sequencing. Peak annotation, *de novo* motif-enrichment analyses, and motif scoring were conducted in *HOMER*. For single-nucleus assay for transposase-accessible chromatin-sequencing (ATACseq), liver nuclei were processed using the Chromium Next GEM Single Cell ATAC Library & Gel Bead Kit v1.1 on the 10x Genomics Chromium controller. Barcode-filtering, clustering and peak calling were done using the *ArchR* pipeline. The stellate cell cluster was identified based on chromatin accessibility in *Lrat*, *Dcn*, and *Reln* loci. The HOMER pipeline was used for motif-enrichment analyses.

Additional details are provided in the supplementary data file and the supplementary CTAT table.

Results

Western diet and fructose-feeding features advanced MASH

Advanced MASH was established in male C57BL/6J mice by feeding a Western diet supplemented with D-fructose in the drinking water for 52 weeks (WD; n = 8). Age-matched control mice (chow; n = 9) were fed chow diet and pure drinking water. WD-fed mice gained weight relative to chow-fed mice and exhibited elevated fasting blood glucose and serum alanine aminotransferase levels indicating insulin resistance and liver injury (Fig. 1A). WD-fed mice exhibited hepatic steatosis and prominent pericellular fibrosis (Figs. 1B,C). We further observed expansions of F4/80-positive macrophages and hepatic αSMA$^+$ cells (Fig. S1A) but saw no indication of myofibroblast proliferation. MASH-specific KI67 staining was cytoplasmic and frequently adjacent to crown-like structures (Fig. S1B). *Mki67* RNA mainly localized to *Clec4f*$^+$ *Trem2*$^+$ cells in crown-like structures, independently of *Itgax*, and occasionally to large cells with round nuclei reminiscent of hepatocytes (Figs. S1C-E). No *Mki67*$^+$/*Dpt*$^+$-activated HSCs (aHSCs) or myofibroblasts were seen (Fig. S1F).

To elucidate molecular changes, we sequenced mRNA from total liver and characterized the proteome. We detected 16,900 transcripts and 5,222 proteins with 4,968 shared features (Fig. 1D). Differences in transcriptomes and proteomes across animals were largely diet-driven (Fig. S1G). Comparing dietary groups, differential expression analyses (*p*.adj. <0.05) revealed 7,230 transcripts and 2,580 proteins (Fig. 1D). In advanced MASH, 434 induced genes and 605 repressed genes showed significant, codirectional changes at the protein level (Spearman rank correlation R = 0.61, *p* <2.2E-16). Differentially expressed genes (DEGs) and proteins (DEPs) belonged to comparable biological processes and pathways (Figs. 1E, S1H). Induced genes were implicated in regenerative and immune system processes (*up*-DEG, *p*.adj. <0.05; Fig. 1E) whereas WD-repressed genes (*down*-DEG, *p*.adj. <0.05) were linked to glucose, lipid, and bile acid metabolic processes (Fig. 1E).

While the differences *between* diet groups dominated, we leveraged the minor differences *within* our WD-fed group to identify processes that covaried. A WGCNA[10] led to 23 co-expression modules (Fig. S1I). Clustering by adjacencies of the module eigengenes gave us seven clusters of modules across our MASH mice (Fig. 1F). Enriched gene ontology (GO) terms for genes in the clusters showed coupling of processes across cell types (Fig. 1G). Some clusters inversely correlated, such as clusters A & G, clusters B & D, and clusters E & F. Clusters B, E, and G relating to nutrient handling, and clusters A, D, and F reflecting zone-3 detoxification processes, regeneration, and inflammation, respectively. W*ithin* co-expression modules we found signature genes of aHSCs, macrophages, and endothelial cells, expression of which covaried tightly across our WD-fed mice (Fig. 1G and not shown). Still, all were significantly induced in WD-fed compared to chow-fed mice and likely represent coupled, MASH-associated processes.

Cell type-resolved analysis of MASH-associated shifts in hepatic gene expression

For a single cell-resolved view, we dissociated livers of 52-week WD- and chow-fed mice (n = 6). We limited the input of hepatocytes and endothelial cells through partial anti-ASGR1 and anti-CD31 immunodepletion and sequenced libraries of live cells (Fig. S2A). The 32,282 cells clustered into 22 Leiden clusters, all containing cells from both conditions (Figs. 2A, B and S2B). From marker gene expression, we identified 10 major hepatic cell types and a population of *Birc5*$^+$ cycling cells (Figs. 2C–E and S2C). In keeping with histology and bulk data, statistical analysis using miloR[11] showed increased abundances of mononuclear phagocytes (MPs), dendritic cells (DCs), T cells/natural killer (NK) cells, and neutrophils. The same was true for *neighborhoods* of mesenchymal and cholangiocyte-like cells whereas other mesenchymal, endothelial and hepatocyte subpopulations were reduced (Fig. 2E *left*).

We next assigned the annotated cell types to the WGCNA modules from our MASH livers. These assignments confirmed our GO analyses (Fig. S2D) and distilled the inverse relationship between normal parenchymal function, inflammation, and regeneration in MASH.

Expression changes within cell populations were prominent in advanced MASH including the repression of Kupffer cell (KC) genes *Cd163* and *Marco*, hepatocyte *Acot1-4*, and hedgehog-associated *Hhip* and *Disp2* in HSCs (Fig. 2F). Major transcriptional increases included the angiogenesis-associated gene *Esm1*, macrophage *Gpnmb*, hepatocyte serum amyloid genes *Saa1/2*, and fibrosis-associated *Col1a1* and *Dpt* in aHSCs. We attributed discrepancies between bulk and cluster-averaged single-cell expression changes to changes in cell stoichiometry *in situ*. This was most apparent for neutrophils, T cells and B cells leading to increased whole liver *S100a8*, *Cd3g*, and *Ly6d* expression. We further subclustered endothelial cells, cholangiocyte-like cells and hepatocytes, NK cells, T cells, DCs, neutrophils, plasma cells and B cells for increased resolution (Figs. S2E-J).

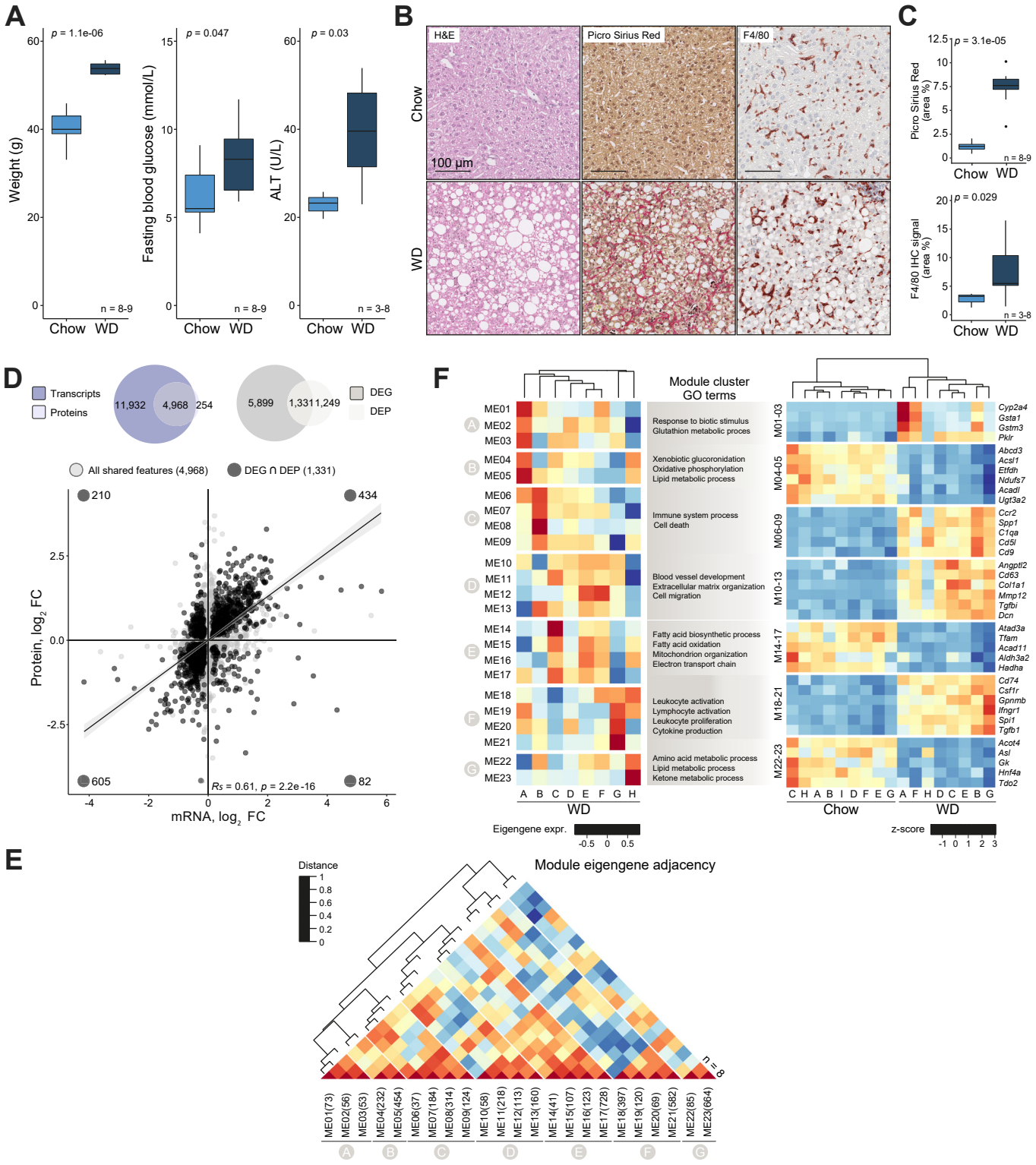

Fig. 1. Murine model of advanced MASH. (A) Body weights, fasting blood glucose, and serum ALT levels of Western diet *vs*. chow-fed mice (Welch's t-tests). (B) H&E, picrosirius red, and F4/80-IHC of liver sections. (C) Picrosirius red and F4/80-IHC signals normalized to tissue area (Welch's t-tests). (D) *Top*, overlap of detected transcripts and proteins, and DEGs (*p*.adj.<0.05, Wald test, Benjamin-Hochberg-corrected) and DEPs. *Bottom*, correlation of log_2FC in mRNA and protein of *shared features* among DEGs and DEPs (dark grey). Spearman rank correlation coefficient *Rs* and *p* value are shown. (E) Western diet WGCNA module eigengene distance plot with adjacency dendrogram. Module sizes shown. (F) Module eigengene expression across WD-fed mice (left). Selected GO terms enriched among DEGs in module clusters (middle) and relative expression of exemplary DEGs (right). All values are means of 3-9 biological replicates. Boxplot vertical bars show data range and horizontal bar median value. DEG, differentially expressed gene; DEP, differentially expressed protein; GO, gene ontology; WD, Western diet; WGCNA, weighted correlation network analysis. (This figure appears in color on the web.)

We inferred gene regulatory networks defining these cell populations in advanced MASH, using SCENIC.[12] Clustering of cells according to regulon activity (AUC) scores led to 12 clusters largely aligned with cell types (Figs. 2G and S2K, L). Marker regulons for each cluster and mean AUC scores for cells herein allowed us to infer cell type- and condition-specific transcription factor (TF) activities (Figs. 2H and S2M). Top TFs predicted to lose activity in resident cells in MASH included HSC lineage-determining factors FOXF1,[13] LHX2,[14] and NR1H4 in mesenchymal cells, HOXA5 in endothelial cells, and the xenobiotic receptor NR1I3/CAR in hepatocytes (Fig. 2H). Developmental and regenerative TFs appeared activated in MASH including GATA6, MECOM, and SOX17 in endothelial and mesenchymal cells, as well as FOXJ1, FOXP2, and HNF1B in the cholangiocyte-like cells. MASH-repressed TF activities within immune cell clusters included MAFB, ETV5, NR1H3 in KCs, and a panel of T cell- and NK cell-enriched TFs including EOMES and STAT4 (Fig. S2M). SPI1/PU.1, CEBPE, and IRF5 were among the most activated TFs within myeloid clusters likely reflecting shifts in cluster composition in MASH.

We recapitulated at single-cell resolution the broad transcriptional changes in advanced MASH. We predicted these changes to be rooted in reset TF activities across cell types, aligning well with the shift from nutrient and xenobiotic handling to inflammatory and wound healing programs observed in our bulk studies.

Liver mesenchyme dynamics in advanced MASH

We subclustered the contiguous mesenchymal population into four clusters of *Lrat*^{hi}/*Rgs5*$^{+}$ quiescent HSCs (qHSCs), *Col1a1*$^{+}$/*Dpt*$^{+}$ aHSCs, fibroblasts, and *Msln*$^{+}$/*Gpm6a*$^{+}$ mesothelial cells (MCs) (Figs. 3A, B). qHSCs of subcluster 1 and 2 mainly came from healthy livers, while aHSCs/fibroblasts of subcluster 3 were derived from MASH livers with the fraction of subcluster-3 cells from chow-fed mice likely representing fibroblasts (Fig. 3C).

We identified subcluster marker genes and tracked their expression across mesenchymal cells and in whole livers from healthy and MASH mice (Figs. 3D and S3A). Markers of aHSCs/fibroblasts related to regeneration and fibrogenesis were induced in MASH livers together with *immediate-early* genes broadly expressed across hepatic cell types. Notably, while expression of qHSC markers were lower in individual aHSCs, several were higher in MASH livers overall (*e.g.*, *Rgs5*, *Reln*, *Lrat*) and others (*e.g.*, *Vipr1* and *Ecm1*) were suppressed. This suggested to us that the expanded population of HSCs was *toned* by the MASH milieu prior to its activation. Expression distributions within subclusters supported this view showing a clear reduction in *Vipr1*^{hi} HSCs among MASH liver-derived subcluster 1-cells whereas *Rgs5* and *Lrat* levels were largely upheld (Fig. 3E). Expression of all HSC markers declined in subcluster-3 and were all but absent in MASH aHSCs. *Dpt* and *Col1a1* expression on the other hand was confined to subcluster 3 and induced in MASH. We confirmed the expansion of HSCs and HSC-derived cells in MASH livers from our *FLEx-TRAP* knock-in mice crossed with the *Lrat-cre* driver line[6] (to express *mCherry-Rpl10a* in HSCs) (Fig. 3F). Despite low recovery of *Acta2*$^{+}$ cells by single-cell RNA sequencing (scRNAseq), αSMA^{+}/mCherry^{+} cells were readily seen in MASH livers, indicating an HSC origin of the activated mesenchyme.

We next delineated the HSC activation trajectory in pseudotime (Fig. 3G). We excluded subcluster-4 MCs, which separated from subclusters 1-3 with only very few cells bridging the two populations (Fig. S3B). A single, unbranched trajectory recapitulated the predicted transition from qHSCs to aHSCs. Focusing on the dominant subclusters 1 and 3, we profiled top highly variable genes (HVGs) over pseudotime (Fig. 3H). This activation trajectory of HSCs in MASH was reminiscent of the HSC trajectory in carbon tetrachloride-induced liver injury, suggesting a common HSC activation mechanism.[2,7]

We applied SCENIC for a focused regulatory network analysis and identification of mesenchymal TFs. AUC-based clustering gave six subclusters (Figs. 3I, *top* and S3C) essentially overlapping our HVG-based clusters (Fig. 3I *bottom left*). Clusters 1 and 2, mainly populated by qHSCs, showed distinctively high activities of LHX2, nuclear receptors NR1H4, NR2F2, NR3C1, RARB, and RXRA as well as ETS1, RELB, NFIB, and SOX5. SCENIC cluster 3 and 4 aHSCs/fibroblasts showed higher activities of SRF, TCF21, HOXB5, KLF9, and HEY1. Yet, TCF21 activity was seen across HSC/fibroblast clusters and decreased in MASH (Figs. 3I and 2H). Cluster 5 MCs were dominated by BHLHE40, WT1, KLF2/4, HLF, DBP, and FOXQ1. High activities of LHX2, NR1H4, NR2F2, NR3C1, and TCF21 regulons yielded to a transient increase in HOXB5 activity and more sustained activity of HEY1 in HVG cluster-1 and -3 cells over pseudotime (Fig. S3E).

Expression of many qHSC signature genes was repressed along the HSC activation trajectory but elevated in whole MASH livers, reflecting an overall increase in MASH-*toned* HSCs. Shifts in TF usage away from nuclear receptors could have driven this transition in response to WD-induced metabolic stress, tissue damage, and altered immune cell activities.

Steady-state dynamics of mononuclear phagocytes

Stellate cell activation co-occurs with profoundly changing macrophage function.[15] By investigating these changes, we expanded on recent reports[16–19] and added important new observations. We subclustered the MP population into nine clusters, capturing its diversity (Fig. 4A). Most MPs recovered from the MASH livers, including monocyte and macrophage subpopulations, rarely found in healthy livers (Fig. 4B). The abundance of embryonically derived *Timd4*$^{+}$ Kupffer cells (emKCs) declined in advanced MASH while *neighborhoods* of *Clec4f*$^{+}$/*Timd4*$^{-}$/*Cd163*$^{-}$/*Marco*$^{-}$ KCs increased (Figs. 4C–E and S4A). This was consistent with impaired emKC self-renewal[17,18] and replacement by monocyte-derived macrophages (MdMs) and KC-like cells (moKCs), but also with emKC re-specification in MASH. The MASH-associated *Clec4f*$^{+}$/*Timd4*$^{-}$ KC population had increased expression of *Clec1b*, *Trem2*, and *Cd63* together with *Cd5l* and *Vsig4*. Notably, also in healthy livers, most *Clec4f*$^{+}$ KCs lacked expression of *Timd4*, *Cd163*, and *Marco* demonstrating an inherent heterogeneity. We hence perceived the three subclusters (1-3) as a continuum of emKCs and *Clec4f*$^{+}$ moKCs adapting to the MASH environment. Subcluster-1 KCs showed the most complete expression of KC markers while subcluster-2 and -3 KCs shared elevated expression of macrophage markers *Cd63* and *Trem2* in the MASH setting (Figs. 4D, E and S4A). A fraction of subcluster-2 KCs expressed *Mmp12*, *Gpnmb* and lipid-handling genes *Lpl*, *Cd36*, and *Fabp5* (Figs. 4D and S4A) while subcluster 3 was signified by higher expression of antigen processing and presentation genes. These included *Cd207* (*Langerin*), *Tmem176b* and MHC class II genes in addition to

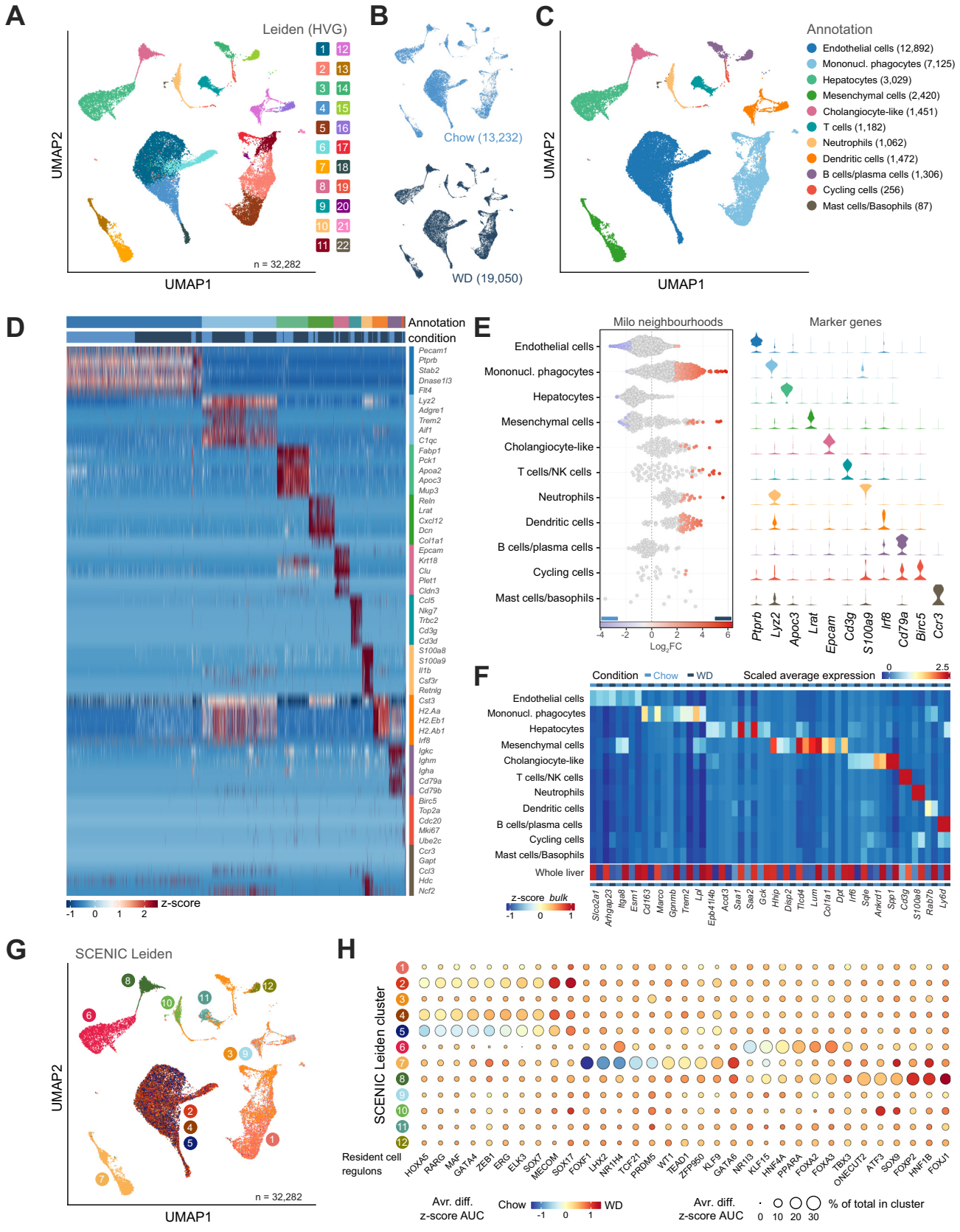

Fig. 2. Single-cell RNA-seq analysis of healthy and advanced MASH livers. (A) UMAP and Leiden clustering of integrated single-cell dataset. (B) Cells split by condition. (C) Annotation of cell populations. Cell counts shown. (D) Scaled expression of marker genes across cells. Cell annotations and conditions shown in horizontal color bars. (E) Left, distribution of log_2FCs across neighborhoods. Differentially abundant neighborhoods at FDR <0.1 are colored (Quasi-likelihood F-test, Benjamini-Hochberg-corrected). Right, Expression of marker genes across populations. (F) Scaled mean expression across annotated populations split by condition.

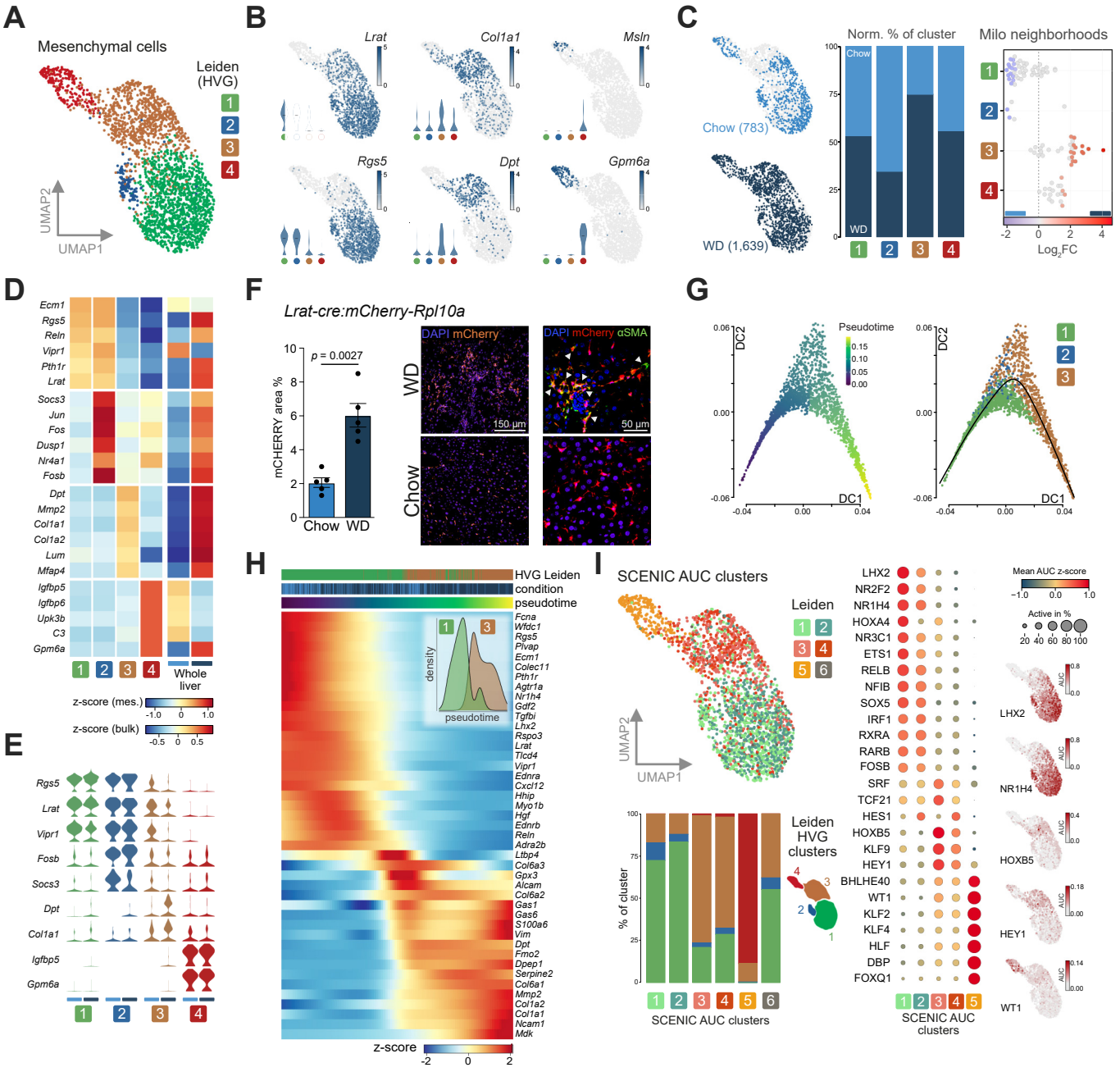

Fig. 3. Mesenchymal cells in healthy and advanced MASH livers. (A) HVG-based UMAP and Leiden clustering of mesenchymal cells. (B) Log_{1p} gene expression and distribution across subclusters. (C) Cells split by condition. Cell counts shown. *Middle*, relative contribution of conditions to subclusters normalized to global cell count for each condition. *Right*, distribution of log_2FCs across neighborhoods. Differentially abundant neighborhoods at FDR <0.1 are colored (Quasi-likelihood F-test, Benjamini-Hochberg-corrected). (D) Scaled mean expression across subclusters and in whole liver (bulk) split by condition. (E) Log_{1p} expression across subclusters split by condition. (F) *Left*, *mCherry*$^+$ HSC area % in livers from chow- and WD-fed *Lrat-cre:mCherry-Rpl10a* mice (Student's *t* test, error bars show standard deviation), *right*, co-detection of mCherry and αSMA. (G) Diffusion maps showing pseudotime variable (*left*) and subclusters 1-3 (right) with *Slingshot* trajectory. (H) *Left*, top 44 variable genes across subcluster 1 and 3 cells ranked in pseudotime. *Insert*, density of subcluster 1 and 3 cells over pseudotime. (I) *Top left*, SCENIC AUC-based Leiden subclusters 1-6 projected onto HVG-based UMAP. *Bottom left*, contribution of each HVG-based subcluster to SCENIC AUC-based subclusters. *Middle*, dot plot of scaled regulon activities. Colors show scaled mean AUC scores for regulons across subclusters. Sizes show fraction of cells in subcluster with regulon activity. *Right*, AUC scores for indicated regulons. AUC, area under curve; DC, diffusion component; FC, fold change; HVG, highly variable genes; mes., mesenchymal subset; UMAP, uniform manifold approximation and projection; WD, Western diet. (This figure appears in color on the web.)

Bottom row shows scaled mean expression in whole liver (bulk). (G) SCENIC AUC-based Leiden clusters 1-12 projected onto HVG-based UMAP. (H) Scaled SCENIC AUC scores for resident cell-associated regulons. Colors show relative regulon activities between conditions. Sizes show regulon activity differences between clusters. AUC, area under curve; FC, fold change; HVG, highly variable gene; UMAP, uniform manifold approximation and projection; WD, Western diet. (This figure appears in color on the web.)

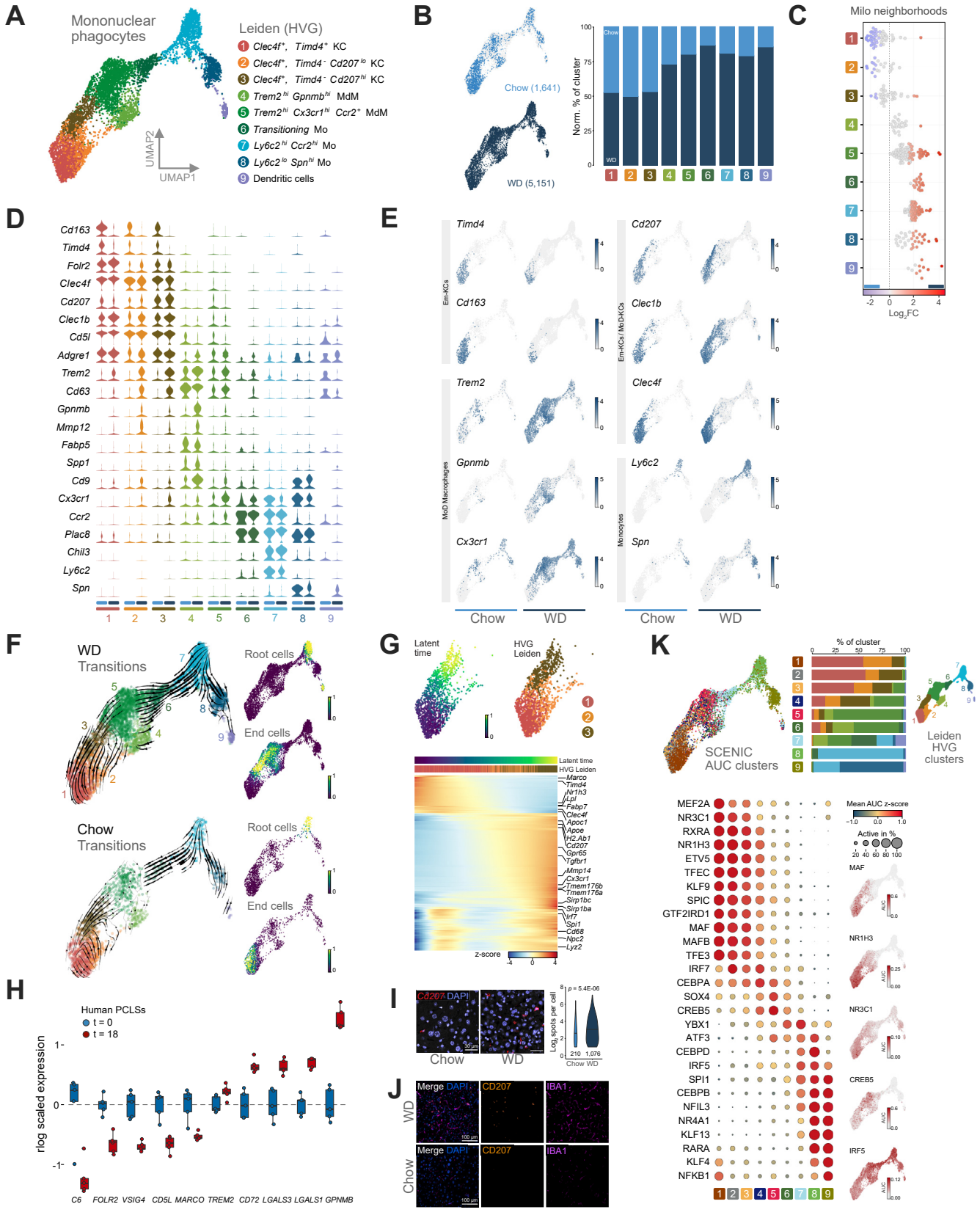

Fig. 4. Mononuclear phagocytes in healthy and advanced MASH livers. (A) UMAP and Leiden clustering of MPs annotated. (B) MPs split by condition. Cell counts shown. *Right*, relative contribution of conditions to subclusters normalized to global cell count for each condition. (C) Distribution of log_2FCs across neighborhoods. Differentially abundant neighborhoods at FDR <0.1 are colored (Quasi-likelihood F-test, Benjamini-Hochberg-corrected). (D) Log_{1p} expression across subclusters stratified by condition. Chow: Light blue, WD: Dark blue. (E) Log_{1p} expression across MP subsets stratified by condition. (F) *Left*, UMAPs of MPs split by condition and overlaid with subclusters and RNA velocities. *Right*, inferred primary *root* and *end* cells. (G) *Top*, scVelo latent time coordinates and subclusters projected onto HVG-

macrophage markers (Fig. S4A) but not DC markers *Flt3*, *Xcr1* or *Clec10a. A Cd207*^{hi} population was detectable in the healthy liver but expanded in MASH.

Besides the reconfiguration of em- and moKCs, advanced MASH was associated with increased numbers of *Ly6c2*^{hi}/*Chil3*^{hi} monocytes, *transitioning* monocytes, and *Spn*$^{+}$ *patrolling* monocytes (Figs. 4D, E; subclusters 6-8). In line with previous reports,[16,20] two *Trem2*^{hi}/*Cd9*$^{+}$/*Cd63*$^{+}$ MdM populations expanded in MASH; subcluster 4 was characterized by *Gpnmb*, *Spp1* (*Osteopontin*) and lipid-handling genes while subcluster 5 retained *Cx3cr1* and *Ccr2* expression and acquired *Mrc1*, *Cd81*, *H2-Ab1*, *H2-Eb1*, and *Tmem176b*. Subcluster-4 MdMs identified as scar-associated macrophages were already present at lower levels in healthy livers. Both MdM subclusters contained *Clec1b*- and *Cd5l*-expressing cells, but the absence of *Clec4f* distinguished these from emKCs and moKCs.

To infer transitions between cell populations in healthy and MASH livers, we applied *scVelo*.[21] MASH liver MPs showed a divergence of the *classical Ly6c2*^{hi}/*Ccr2*^{hi}/*Chil3*^{hi} monocytes into *Spn*^{hi} patrolling monocytes and the two *Trem2*^{hi} MdM populations through a transient, *Ly6c2*^{lo}/*Ccr2*^{hi} and MHC class II-positive monocyte state (Fig. 4F). Among scar-associated macrophages, the induced *top-likelihood* genes *Gpnmb*, *Elovl1*, *Fabp5*, *Trem2*, and *Lamp2* pointed towards increased phagocytotic capacities (Figs. 4F and S4B). Meanwhile, specifically *Cx3cr1*^{hi}/*Mrc1*^{hi}/*Cd81*^{hi} MdMs transitioned further into the *Cd207*^{hi} population of subcluster 3 predicted as the main, MASH-specific endpoint. During this transition, expression of *Clec4f*, *Cd5l*, and *Vsig4* emerged while that of *Cxc3r1*, *Ccr2,* and *Itgax* was lost.

Importantly, we further predicted the convergence of *Clec4f*^{hi} subcluster-1 KCs with this *Cd207*^{hi} KC-like subcluster 3 in MASH. Dynamic expression of KC-enriched genes (*Cd5l*, *Clec1b*, *Apoc1*, *Wfdc17*, and *C6*) accompanied their transition in concert with induction of *Apoe*, *Mrc1*, *Nedd8*, and *Vcam1* (Figs. 4F and S4B). A focused delineation of the transition from subcluster 1 to 3 supported *Cd207*^{hi} cells being a likely *end-state* in murine MASH (Fig. 4G). In cultured precision-cut liver slices from a healthy human donor undergoing *ex vivo* wound healing, MP transitions were uncoupled from the influx of monocytes yet showed a swift repression of KC signature genes and induction of activation markers including *TREM2* and *GPNMB* (Fig. 4H).

CD207 was previously found to be a marker of capsule macrophages[22] but in advanced murine MASH, CD207^{+} cells populated the parenchyma (Figs. 4I, J). While GPNMB^{+}/*Trem2*$^{+}$ MdMs were frequently observed in hepatic crown-like structures, *Cd207*^{hi}/*Trem2*$^{+}$ KC-like cells were rarely found in them (not shown). Their high expression of *Slc40a1*, *Igf1*, and immunomodulatory *Irf7*, *Il18bp*, and *Hpgd* could point to inflammation-resolving functions. In the healthy liver, transition of low numbers of *Ly6c2*^{hi} monocytes through subclusters 5 and 3 towards *Timd4*^{hi} *end cells* (Fig. 4F) indicated a steady-state monocyte contribution to the hepatic MP population (Fig. 4I, J).

To infer transcriptional drivers, we again turned to SCENIC. Nine AUC score-based subclusters were identified (Figs. 4K, *left*, and S4D-E). SCENIC inferred high activities of NR1H3, MAF, MAFB, TFEC, and SPIC across the KC-rich clusters 1-4 (Figs. 4K and S4F). The broad profile of NR1H3 would fit with dual roles in *Clec4f*$^{+}$/*Timd4*$^{+}$ KCs specification and adaptation to injury.[17,23] Glucocorticoid receptor NR3C1 and MEF2A activities were more confined to subcluster-1 KCs from healthy livers, whereas active IRF7 and C/EBPα marked cells of subclusters 2-4 with a larger fraction of KCs from MASH livers. The monocyte-rich subclusters 7-9 were dominated by PU.1 (SPI1), C/EBPβ, C/EBPδ, and NFIL3 whose predicted activities dropped steeply in MdMs.

Inference of the steady-state transitions of MPs in healthy liver and MASH showed the convergence of liver-resident emKCs and MdMs in *Timd4*^{hi} and *Cd207*^{hi} *end populations*, respectively. Proof of the contribution of both emKCs and monocytes to the latter population in advanced MASH will require lineage tracing.

HSC NR1H4 activity is associated with quiescence

Having seen extensive transcriptional reconfiguration of mesenchymal and MP populations, we next predicted specific interactions between these populations in healthy livers and advanced MASH (Fig. 5A). Among the predicted, mesenchyme-derived ligands with top activities were the BMPs (GDF2/BMP9, BMP5, and BMP10) signaling autocrinally through receptors ALK3 (*Bmpr1a*) and BMPR2 or to KCs/MdMs through ACVR2A and ALK1 (*Acvrl1*). Most mesenchyme-derived ligands were abundantly expressed in qHSCs and repressed in aHSCs/fibroblasts. Strongly qHSC-enriched ligands with predicted effects on MPs further included CXCL12, CDH2, NRXN1, MAPT, IL34, HGF, and NTN1, as supported by visualization of expression patterns across HSC clusters (Fig. 5B). Given the importance of GDF2 in the specification of KCs and liver sinusoidal endothelial cells (LSECs),[24,25] we validated our observations *in situ,* demonstrating reduced per-cell *Gdf2* transcript levels in MASH livers (Fig. 5C). Along with *VIPR1* and other qHSC markers, expression of *GDF2* was also strongly reduced in human precision-cut liver slices as they underwent *ex vivo* wound healing (Fig. 5D).

We revisited predicted target genes in our HSC SCENIC analysis and found *Gdf2* as a putative NR1H4 target gene. The association of NR1H4 with HSC quiescence sparked our interest, as NR1H4 agonists like OCA are antifibrotic in humans and mice.[26,27] We therefore transcriptionally profiled primary murine HSCs treated with OCA for 6 h. Culturing induces HSC activation, but OCA preserved expression of the key quiescence-associated genes *Lhx2*, *Lrat*, *Hhip*, and stimulatory G_S-protein-coupled receptors (G_SPCRs) in addition to *Gdf2*, *Bmp10*, *Angptl6* and other *stellakines* (Fig. 5E and not shown). aHSC-associated genes *Col1a2*, *Ccn2*, *Alcam*, *Aebp1*, and *Mmp10* were repressed. OCA hence had quiescence-preserving activity

based UMAP of MASH liver-derived MPs. *Bottom*, scaled expression of top 210 variable genes across subclusters 1-3. Latent time coordinates and subcluster annotation shown in top color bars. (H) Rlog-transformed, scaled expression of selected DEGs in precision-cut human liver slices (*p*.adj. <0.005, n = 5, Wald test, Benjamini-Hochberg-corrected). Boxplot vertical bars show data range and horizontal bar median value. (I) *Cd207* mRNA in livers from chow- and WD-fed mice, spot quantification (right) with indication of total number of positive cells (n = 10-12 frames, Wilcoxon rank-sum test). (J) CD207, IBA1 protein in livers from chow- and WD-fed mice. (K) *Top left*, SCENIC AUC-based Leiden subclusters 1-9 projected onto HVG-based UMAP. *Top right*, relative contribution of each HVG-based subcluster to SCENIC AUC-based subclusters. *Bottom left*, dot plot of scaled MP regulon activities. Colors show scaled mean AUC score for regulons across subclusters. Sizes show fraction of cells in subcluster with regulon activity. *Bottom right*, AUC scores for indicated regulons. AUC, area under curve; FC, fold change; HVG, highly variable genes; PCLS, precision-cut liver slices; UMAP, uniform manifold approximation and projection; WD, Western diet. (This figure appears in color on the web.)

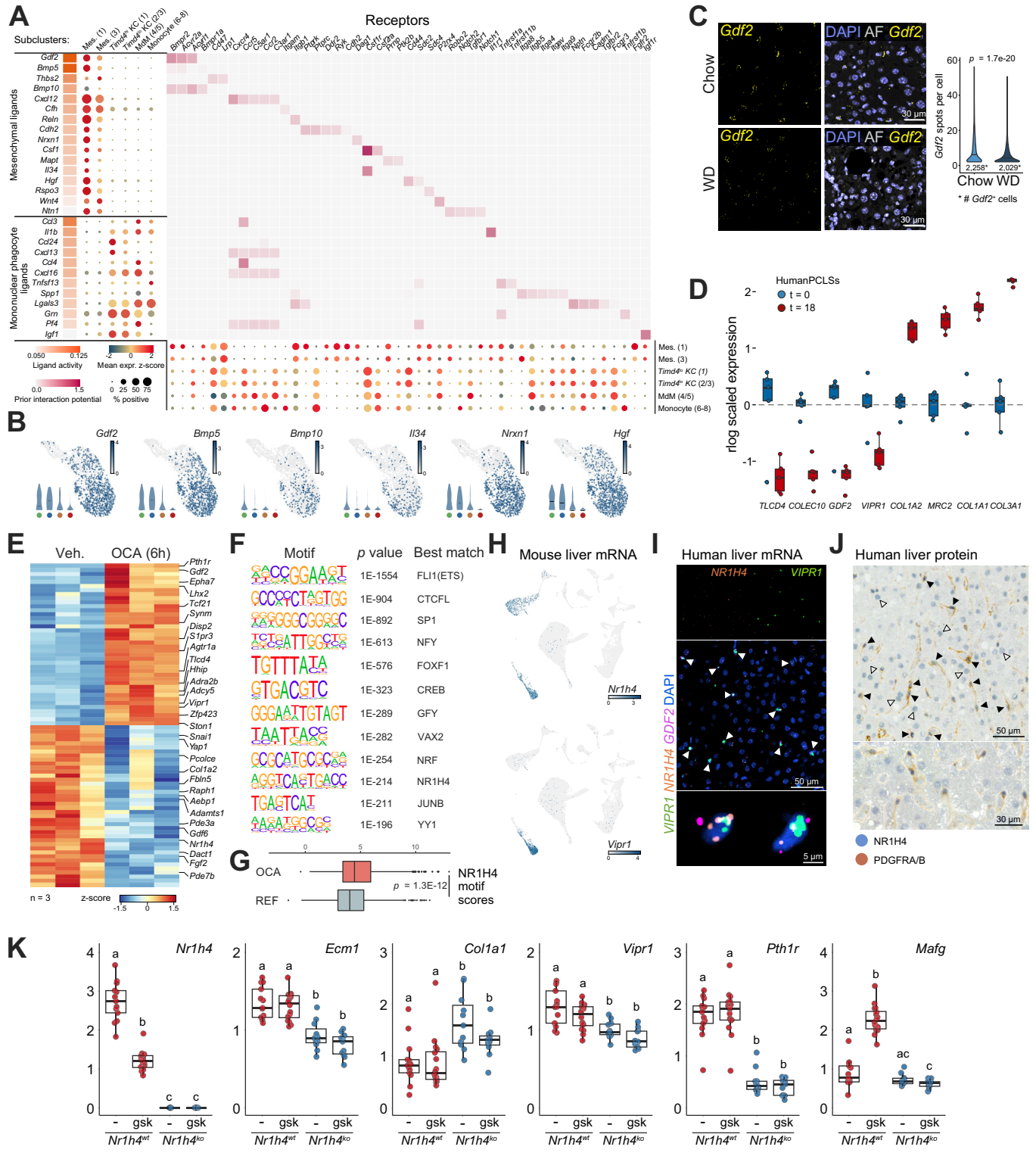

Fig. 5. NR1H4 expression and activity in hepatic stellate cells. (A) NicheNet analysis of inferred ligand-receptor interaction potentials between mesenchymal cells (Mes.) and MP subclusters. Dot plots show ligand (*left*) and receptor expression (*bottom*). Colors show scaled mean expression across subclusters. Sizes show fraction of expressing cells in subcluster. (B) Log_{1p} expression values of selected HSC ligands and distribution across mes. subclusters. (C) *Gdf2* mRNA in livers from chow- and WD-fed mice, spot quantification (*right*) with indication of total number of positive cells (n = 10-12 frames, Wilcoxon rank-sum test). (D) Rlog-transformed, scaled expression of selected DEGs in precision-cut human liver slices (*p*.adj. <0.005, n = 5, Wald test, Benjamini-Hochberg-corrected). (E) Scaled mean expression of selected DEGs (*p*.adj. <0.05, Wald test, Benjamini-Hochberg-corrected) in HSCs treated for 6 h with OCA (5 μM) or DMSO (Veh.)(n = 3). (F) Top enriched *de novo* motifs within accessible chromatin in HSCs from *FLEx-TRAP* mice with indication of best matching known motif. (G) Wilcoxon rank-sum test of log-odds NR1H4 motif scores in peaks within +/- 25 kb of TSS of 410 OCA-induced genes *vs.* randomly sampled peaks. (H) Log_{1p} expression in global dataset. (I) *VIPR1*, *NR1H4*, and *GDF2* mRNA in human liver. Magnification of representative cells (*bottom*). (J) NR1H4 (SG, blue) and PDGFR (DAB, brown) IHC in human liver show $NR1H4^{+}$/$PDGFR^{+}$ HSCs (black arrows) and $NR1H4^{+}$/$PDGFR^{-}$ hepatocytes (open arrows). (K) Normalized expression in livers from $Nr1h4^{wt}$ and $Nr1h4^{ko}$ mice treated with vehicle (-) or GSK2324 for three days. Differential expression is indicated by different letters (FDR <0.05, Benjamini-Hochberg-corrected pairwise Wilcoxon Rank Sum tests). Boxplots (D and K), vertical bars show data range and horizontal bar median value. AF, autofluorescence; gsk, GSK2324; KC, Kupffer cells; MdM, monocyte-derived macrophages; Mes.; mesenchymal cells; OCA, obeticholic acid; PCLSs, precision-cut liver slices; REF, reference genes; Veh., vehicle; WD, Western diet. (This figure appears in color on the web.)

directly on HSCs beyond what was previously reported. Direct NR1H4 transactivation would reflect in accessible NR1H4 IR1 binding motifs in HSC chromatin. To test this, we isolated *mCherry*-tagged nuclei from livers of our *FLEx-TRAP* mouse line and performed ATACseq. The NR1H4 motif was strongly enriched ($p = 1E^{-214}$) in HSC ATACseq peaks found in intronic, intergenic, and promoter-proximal genomic regions (Figs. 5F and S5B). Among the most enriched motifs were also motifs for the HSC lineage-associated ETS-family, CREB, FOXF1, and NRF. Within peaks near (+/-25 kb) transcriptional start sites of OCA-induced genes, the NR1H4 IR1 motif was the top enriched motif ($p <1E^{-41}$, Fig. S5C) and with higher log-odds motif scores relative to randomly sampled peaks elsewhere (Fig. 5G). Consistent with direct regulation, peaks with NR1H4 binding motifs were found in the vicinity of the OCA-induced qHSC genes *Vipr1*, *Pth1r*, *Lhx2*, and *Des*. Co-enrichment of the ETS-family binding motif in NR1H4 motif-containing peaks (not shown) could explain the HSC-selective effects of OCA. We corroborated our findings from genetically labeled HSCs by single-nuclei ATACseq analysis of mesenchymal nuclei. Again, the NR1H4 IR1 motif was highly enriched within HSC peaks ($p = 1E^{-67}$) and topped the list of enriched motifs in peaks near OCA-induced genes ($p <1E^{-20}$) (Figs. S5D-E).

We confirmed HSC-specific co-expression of *Nr1h4* and *Vipr1* in our scRNAseq dataset (Fig. 5H) and validated this in human liver (NAFLD activity score [NAS] 2) *in situ* (Fig. 5I). Here, *VIPR1*-expressing cells co-expressed *NR1H4* and *GDF2* whereas *NR1H4*$^+$/*VIPR1*$^-$ cells had large, round nuclei distinctive of hepatocytes. *NR1H4* and *VIPR1* were co-expressed with *LUM,* further indicating that *NR1H4*$^+$/*VIPR1*$^+$ cells were HSCs (Fig. S5F). *NR1H4* and *VIPR1* more abundant in healthy liver (NAS 0) while *LUM* levels increased in MASH (NAS 7). Human snRNAseq data (GSE212837)[28] corroborated HSC *LUM* expression in both healthy and MASH livers (Fig. S5G). Importantly, the NR1H4 protein was also particularly abundant in PDGFR$^+$ mesenchymal cells (likely HSCs) lining the human liver sinusoids (Fig. 5J).

In vivo stimulation of HSC NR1H4 by OCA in mice has proven difficult. Either due to high levels of endogenous ligands or because of modification rendering it refractory to OCA activation.[29] We instead quantified gene expression in livers of wild-type or *Nr1h4* null mice acutely treated with the selective NR1H4 agonist GSK2324 or vehicle.[8] Like OCA, GSK2324 had no acute effect on qHSC-expressed *Ecm1*, *Vipr1*, *Pth1r*, nor *Col1a1 in vivo* (Fig. 5K). *Mafg*, expressed by both HSCs and hepatocytes, was readily induced, and *Nr1h4* was repressed as seen in HSCs *in vitro*. Nevertheless, loss of NR1H4 significantly reduced expression of *Ecm1*, *Vipr1*, and *Pth1r*, while *Col1a1* expression was elevated. These findings were consistent with our scRNAseq studies and with NR1H4 upholding HSC quiescence *in vivo*. We found comparable albeit less pronounced changes in our analysis of liver microarray data from *Nr1h4* null mice bred independently elsewhere (Fig. S5H).[30]

The HSC as a sinusoidal signaling nexus

G_SPCR genes *Vipr1* and *Pth1r* were repressed in aHSCs along with other GPCRs and auxiliary factors *in vivo* and *in vitro* (Fig. 6A, not shown). This together with the OCA-induced increase in *Vipr1* and *Pth1r* expression prompted us to examine HSC cAMP signaling at the transcriptomic level. To profile the cAMP response independently of receptor levels we treated murine HSCs with forskolin (5 μM, 3 h). Besides induction of canonical CREB targets and repression of hippo pathway-regulated genes, cAMP increased expression of defining genes for qHSC function including *Foxf1*, *S1pr3*, *Hhip*, *Gdf2,* and *Hgf* (Fig. S6A). We next investigated the sustained effects of cAMP signaling in HSCs 24 h after the 3 h stimulation with forskolin. Consistent with phenotype-preserving effects of cAMP signaling, qHSC gene expression was upheld while activation-associated genes were suppressed (Fig. 6B). This is reflected in the enriched GO categories including differentiation processes and immunomodulation (Figs. 6C and S6B). Accordingly, cAMP-induced genes were abundantly expressed in qHSC subclusters 1 and 2 compared to aHSCs/fibroblasts of subcluster 3 where cAMP-repressed genes were prominent (Fig. 6D). Bile acids and VIP are both elevated in portal circulation postprandially. Having seen OCA-induced G_SPCR expression, we stimulated primary HSCs with OCA prior to VIP to potentiate its effects. In keeping with this notion, pre-stimulation with OCA enhanced the stimulatory effects of VIP on qHSC genes and repression of HSC activation genes (Fig. 6E).

Systemic effects of VIP complicate targeting of HSC-specific VIPR1 *in vivo*. We therefore applied a chemogenetic strategy expressing the eGPF-tagged *G_S-coupled designer receptor exclusively activated by designer drugs* (G_SD)[5] in HSCs for ligand-induced cAMP signaling with the otherwise biologically inert ligand DCZ (deschloroclozapine). We confirmed the eGFP signal specifically in *Des*$^+$ HSCs of *Lrat-cre*:G_SD but not in cre-negative littermates (Fig. S6C). We next fed these mice (n = 3) the GAN diet for 12 weeks to invoke obesity and massive hepatic steatosis (Fig. S6D). No differences between genotypes were seen. After 3 days with daily oral doses of DCZ (0.1 mg/kg), we found *Gdf2* and *Nr4a1* cre-dependently induced in *Lrat*$^+$ HSCs recapitulating our findings from isolated HSCs *in vivo* in the context of steatotic liver disease (Figs. 6F and S6E). Longer term studies will show if HSC-specific cAMP signaling has sinusoid-preserving and antifibrotic effects *in vivo*.

Combined, our findings feature HSCs as integrators and conveyors of postprandial signals. Further, they point to the phenotypic preservation of qHSCs as a possible direct antifibrotic effect of NR1H4 activation and to the therapeutic potential of HSC-directed treatment to preserve liver sinusoidal health.

Discussion

In the current study, we fed mice a Western diet supplemented with fructose for 52 weeks to recapitulate human MASH. Steatosis, hepatocyte damage, massive expansion of the F4/80^{hi} macrophage population, and extensive pericellular fibrosis were accompanied by major alterations in gene and protein expression revealing process-coupling across hepatic cell populations. Resolving individual cell populations by scRNA-seq allowed us to further explore transitions of cell types and crosstalk between them. This led us not only to the elucidation of novel cellular dynamics in both MASH and in healthy livers, but also to the discovery of a NR1H4-G_SPCR-GDF2 signaling module that may be exploited therapeutically.

In MASH, HSCs, the main cell type implicated in ECM production, underwent repression of nuclear receptor gene programs conferring pericyte identity including GPCR expression. One of these nuclear receptors, NR1H4, is a promising target for

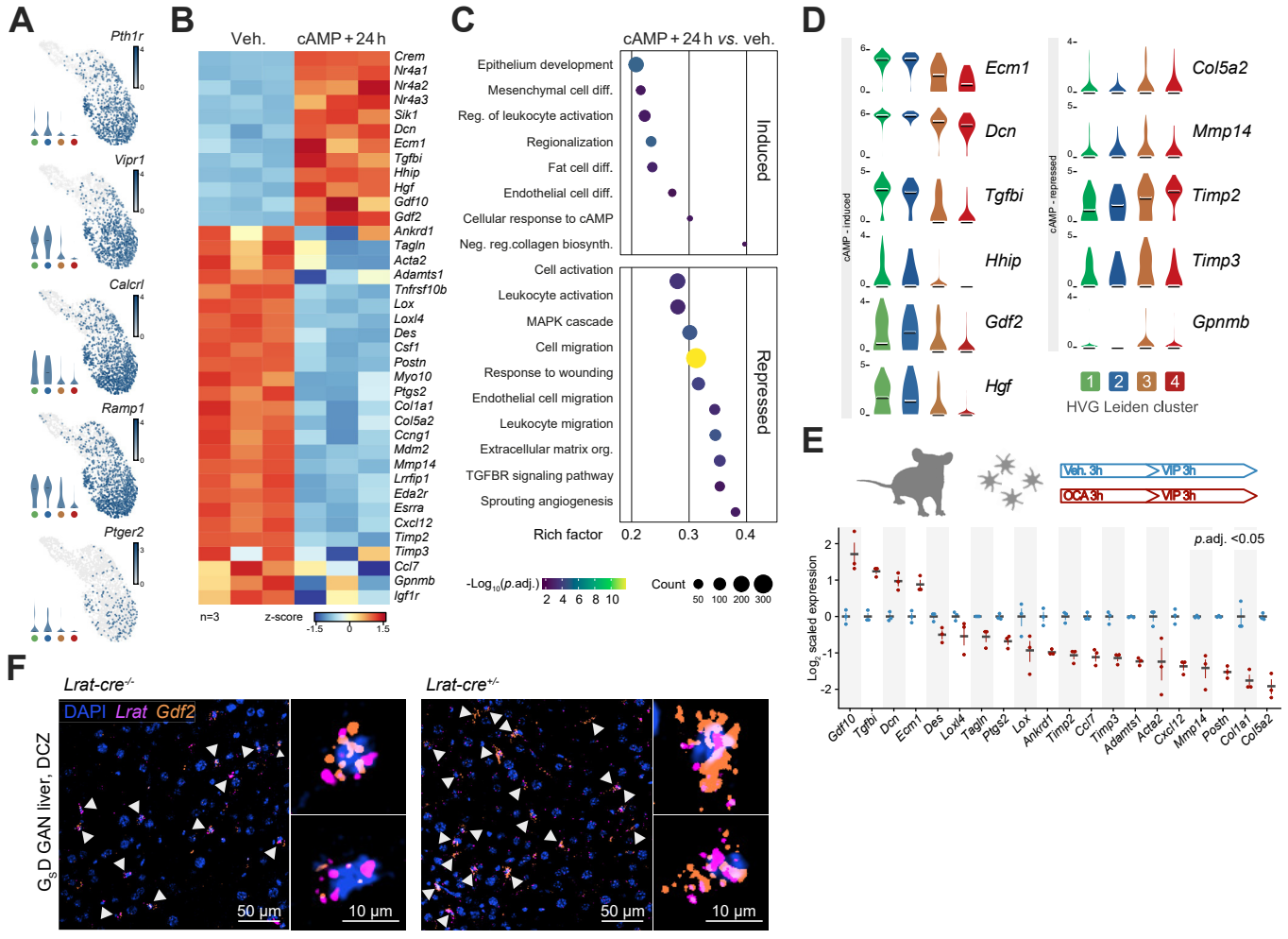

Fig. 6. Hepatic stellate cells as sinusoidal signaling hub. (A) Log_{1p} gene expression and distribution across mes. subclusters. (B) Scaled mean expression of selected DEGs (*p*.adj. <0.05, Wald test, Benjamini-Hochberg-corrected) in primary murine HSCs 24 h after acute cAMP-stimulation (5 µM forskolin, 3 h) or DMSO (Veh.). (C) Selected GO terms enriched among OCA-induced and repressed DEGs. Rich factors, $-log_{10}$(*p*.adj.), and DEG counts within categories are shown. (D) Log_{1p}-expression of selected DEGs across mes. subclusters. Medians shown. (E) Log_2-normalized, scaled expression of selected DEGs (*p*.adj. <0.05, Wald test, Benjamini-Hochberg-corrected) in primary murine HSCs treated with VIP (500 nM, 3 h) after pretreatment with OCA (5 µM, 3 h) or DMSO. Dotplot vertical bars show standard deviations and horizontal bars means. (F) *Lrat* and *Gdf2* mRNA in livers of G_sD and Lrat-cre:G_sD mice (n = 3) fed GAN diet for 12 weeks and treated for three days with DCZ (0.1 mg/kg). Small images show magnifications of representative cells. DCZ, deschloroclozapine; GSD, GSDREADD transgenic; HVG, highly variable genes; OCA, obeticholic acid; Veh, vehicle (DMSO); VIP, vasoactive intestinal peptide. (This figure appears in color on the web.)

antifibrotic therapy.[26,31] NR1H4 agonists may directly oppose HSC activation[29,32] but the expression and function of NR1H4 in HSCs have been questioned.[33–35] We found NR1H4 highly expressed in human and murine qHSCs as the sole non-parenchymal cell type and inferred high NR1H4 activity in qHSCs by ATACseq and SCENIC analyses. Paralleling *Foxf1* and *Lhx2*, the expression and inferred activity of *Nr1h4* in HSCs were diminished in MASH, whereas OCA induced qHSC markers and *stellakines* including *Gdf2*, *Angptl6*, and *Bmp10*. OCA also induced the expression of G_SPCR genes *Vipr1* and *Pth1r* thereby priming HSCs for cAMP signaling. Why treatment with NR1H4 agonists *in vivo* fails to further stimulate qHSC markers despite high NR1H4 expression is unclear. It is possible that NR1H4, unliganded or activated by endogenous ligands, upholds qHSC gene expression in the healthy liver via cooperation with, for example, ETS1 and FOXF1. Posttranslational modifications could also modulate NR1H4 activities *in vivo*.[29] Refined studies are needed to understand HSC-specific NR1H4 activation in appropriate disease contexts.

Intriguingly, *Nr1h4* null mice are protected against bile duct ligation (BDL)-induced hypercholemia and fibrosis.[33] Similarly, mice lacking *Nr1h4* in HSCs show less BDL-induced fibrosis and a tendency towards lower circulating alanine aminotransferase and bile acid levels,[36] arguing that either HSC NR1H4 links sinusoidal bile acid accumulation to HSC activation or itself contributes to cholestasis. Disease context and dosage of NR1H4 ligands may explain the contrast to the HSC quiescence-preserving effects of NR1H4 in our current study. Further, BDL-associated fibrosis in mice is generally attributed to the activation of portal fibroblasts expressing neither *Nr1h4* nor *Lrat*.[37,38] Constitutive ablation of *Nr1h4* in HSCs could hence impact other mesenchymal populations, the interplay of which is incompletely understood. Notably, *Nr1h4* null mice are not protected against carbon tetrachloride- nor Schistosoma-induced liver fibrosis.[33,39]

OCA has not previously been demonstrated to phenotypically preserve HSC identity and sensitize towards G_SPCR agonism. Curiously, NR1H4 does induce *Vipr1* in gallbladder epithelium

where VIP promotes choleresis through increased electrogenic bicarbonate secretion.[40] While the function of HSC-expressed solute carriers is underexplored, the regulatory similarity raises the interesting possibility that HSC-specific VIPR1, by augmenting sinusoidal blood flow, also affects peribiliary vascular drainage and postprandial bile acid transport from the liver.

G_SPCRs like VIPR1 are abundant in HSCs and promote their postprandial relaxation. Ablation of NR1H4 or development of MASH led to striking repression of *Vipr1*. To test if VIPR1-induced cAMP signaling was linked to HSC quiescence, we induced cAMP production in isolated HSCs and recorded effects on gene expression. Acute stimulation increased expression of quiescence markers including *Hhip*, *Gdf2*, *Hgf*, *S1pr3*, and *Foxf1*. Sustained effects of transient cAMP-elevation included repression of ECM genes and myofibroblast markers in addition to preservation of the qHSC program. Follow-up experiments will determine if these effects depend on FOXF1 and if selective elevation of cAMP in HSCs *in vivo* can blunt or even reverse their activation. Transient, chemogenetic elevation of cAMP in HSCs *in vivo* markedly elevated *Gdf2* expression, confirming the signaling module revealed by our scRNAseq and *in vitro* studies. An anti-inflammatory and antifibrotic outcome of cAMP signaling in HSCs would be in line with effects in other pathologies.[41–43]

Transcriptional regulators we predicted lose activity upon HSC activation also include nuclear receptors NR2F2, NR3C1, RARB, and RXRA as well as ETS1, IRF1, and SOX5. NR2F2 is abundant in HSCs and LSECs and instrumental for retinoic acid signaling during development[44] but has also been implicated in the liver injury response.[45] ETS1 and IRF1 were recently proposed as HSC lineage-determining factors,[46] whereas SOX5 is critical for neurogenesis and chondrocyte specification.[47,48] Given its putative role in chondrocyte collagen expression, we speculate that SOX5 and possibly NR2F2 maintain accessible chromatin around both quiescence- and repair-associated genes to ensure HSC plasticity and immediate response to injury. We previously proposed a similar role for ETS1.[7]

The steady-state fluxes of MPs of embryonic and monocyte origin expanded and rerouted in advanced MASH. Different environments clearly guided MdMs as they transitioned towards moKCs in healthy and MASH livers. In advanced MASH, *activated* emKCs and *Cx3cr1*^{hi} MdMs appeared to converge towards *Cd207*^{hi}/*Trem2*^{hi} KC-like cells. Activation of emKCs in advanced MASH involved loss of *Timd4*, *Cd163,* and *Marco* expression also seen at earlier disease stages.[17] We did not experimentally validate the mixed emKC and MdM origin of the *Cd207*^{hi} population, and a contribution from emKCs contrasts with recent reports that *Trem2*$^{+}$ KC-like cells in less advanced, murine MASH are entirely monocyte derived.[18,20] CCR2 is critical for monocyte extravasation at sites of inflammation. In elegant studies of mice fed a fibrogenic diet, Daemen *et al.*[20] observed little reduction in the TIM4^{lo} KC population in *Ccr2*$^{-/-}$ mice despite steep declines in liver Ly6C^{hi} monocytes and CX3CR1^{hi} MdMs. Notably, the *Ccr2*$^{-/-}$ mice showing near-normal levels of TIM4^{lo} KCs all had markedly lower levels of TIM4^{hi} KCs. Whether accelerated loss of resident TIM4^{hi} emKCs in these mice had opened the niche to *Ccr2*$^{-/-}$ monocytes escaping the recruitment block, or if reduced monocyte infiltration led more activated emKCs to contribute to the TIM4^{lo} population remains unclear. The repression of HSC *Gdf2* and *Bmp10* in MASH presented here may contribute to sinusoidal phenotypic transition. GDF2-ALK1 and GDF2-BMPR2 signaling is crucial for KC and LSEC specification, respectively,[24,25,49] and missing input from HSCs may accelerate deterioration of the sinusoidal niche.[19] Such a shift from qHSCs upholding sinusoidal specialization to fibrogenic aHSCs is reminiscent of their transition from HGF-producing suppressors of hepatocarcinogenesis to tumor-promoting myofibroblasts[50] upon activation. This highlights the wider prospects of therapeutic preservation of HSC quiescence in chronic liver disease.

Our study establishes a conceptual framework where signals preparing the liver sinusoid for the postprandial state concurrently promote its phenotypic stability through transcriptional networks and paracrine mediators. Within this framework, HSCs emerge as a nexus for the integration and transmission of physiological signals sustaining sinusoidal homeostasis. In advanced MASH, ongoing parenchymal damage, inflammation, and HSC activation may drive sinusoidal deterioration both through fibrogenesis and by desensitization to these physiological cues. Therapeutic utilization of this pericyte signaling module may on the other hand restore liver sinusoidal homeostasis.

Affiliations

[1]*Department of Biochemistry and Molecular Biology, University of Southern Denmark, Denmark;* [2]*Department of Pharmaceutical Technology and Biopharmacy, University of Groningen, The Netherlands;* [3]*Department of Gastroenterology and Hepatology, Odense University Hospital, Esbjerg Denmark;* [4]*Department of Gastroenterology and Hepatology, University Hospital of South Denmark, Esbjerg Denmark;* [5]*Department of Pathology, Odense University Hospital, Denmark;* [6]*Department of Molecular Medicine, University of Southern Denmark, Denmark;* [7]*Department of Nephrology, Odense University Hospital, Denmark;* [8]*Department of Integrative Biology and Pharmacology, McGovern Medical School, UT Health Houston, USA;* [9]*Department of Medicine, Division of Cardiology, University of California, Los Angeles, USA;* [10]*Department of Biological Chemistry, David Geffen School of Medicine, University of California, Los Angeles, USA;* [11]*Department of Clinical Research, University of Southern Denmark, Denmark;* [12]*Center for Functional Genomics and Tissue Plasticity, University of Southern Denmark, Denmark*

Abbreviations

aHSC, activated hepatic stellate cell; ATAC, assay for transposase-accessible chromatin; BDL, bile duct ligation; DC, dendritic cell; DEG, differentially expressed gene; emKC, embryonically derived Kupffer cell; GPCR, G-protein-coupled receptor; GsD, Gs-coupled designer receptor exclusively activated by designer drugs; GsPCR, Gs-protein-coupled receptor; HSC, hepatic stellate cell; HVG, highly variable gene; KC, Kupffer cell; LSEC, liver sinusoidal endothelial cell; MdM, monocyte-derived macrophage; moKC, monocyte-derived Kupffer cell; NAS, NAFLD activity score; NK, natural killer; MASH, metabolic dysfunction-associated steatohepatitis; OCA, obeticholic acid; qHSC, quiescent hepatic stellate cell; scRNAseq, single-cell RNA sequencing; VIP, vasoactive intestinal peptide; WD, Western diet supplemented with D-fructose in the drinking water; WGCNA, weighted correlation network analysis.

Financial support

S.M.B., M.K.T., P.H., F.T.L., C.W.W., M.M.L., A.K., L.G., B.B., and K.R. were supported by the Danish National Research Foundation (grant DNRF141) to Center for Functional Genomics and Tissue Plasticity. DH, KHH, and TVD recieved scholarships from the Danish Diabetes Academy, funded by the Novo Nordisk Foundation (grant NNF17SA0031406). KR was supported by a project grant (#1030-00390B) from the Independent Research Fund Denmark. Proteomics work was supported by the Novo Nordisk Foundation (NNF18OC0052768 and the INTEGRA research infrastructure). T.Q.d.A.V. are sponsored by NIH grant DK118064. Bioimaging was performed at DaMBIC, a bioimaging research core facility, at the SDU established by a grant from The Danish Agency for Science, Technology and Innovation and intramural funding.

Conflict of interest

The authors declare no competing interests.

Please refer to the accompanying ICMJE disclosure forms for further details.

Authors' contributions

Conceptualization, S.M.B. and K.R.; Methodology, S.M.B., M.K.T., and K.R.; Formal Analyses, S.M.B., P.R.S., M.K.T., D.H., F.A.B., A.P.T., N.G.E., P.H., T.V.D, F.T.L., J.V., E.A.H.S., A.M., S.D., L.G., H.D., T.Q.d.A.V., and K.R.; Resources, C.W.W., S.D., L.G., H.D., M.M.L., A.K., B.B., R.B., T.Q.d.A.V., and K.R.; Writing - Original Draft, S.M.B., and K.R.; Writing - Review & Editing, S.M.B., D.H, C.W.W., P.R.S, K.H.H., P.H., S.D., and KR; Supervision, S.D., L.G., H.D., M.M.L., A.K., B.B, and K.R.; Project Administration, K.R., Funding Acquisition, K.R.

Data availability statement

Transcriptomics and chromatin accessibility data generated in this study is available in Superseries GSE218300 in the NCBI Gene Expression Omnibus repository. Mass spectrometric data is available at ProteomeXchange consortium via the PRIDE partner repository with data set identifier PXD045269. Analysis code is placed on the Ravnskjaer-lab Github page.

Acknowledgements

We thank Tenna P. Mortensen, Maibrith Wishoff, Ronni Nielsen, Morten F. Ebbesen, Inger Nissen (University of Southern Denmark (SDU)), and Angela Cheng (University of California, Los Angeles) for technical assistance. We thank Robert F. Schwabe (Columbia University) for the Lrat-cre mouse strain. We further thank Birgitte Gade Jacobsen, Lea Ladegaard Grønkjær (University Hospital of South Denmark) for assistance with human liver tissue, Lone Christiansen for assistance with handling and special staining, and Tina Di Caterino (SDU) for its pathological evaluation.

Supplementary data

Supplementary data to this article can be found online at https://doi.org/10.1016/j.jhep.2023.11.001.

References

Authors names in bold designate shared co-first authorship

[1] **Dobie R**, **Wilson-Kanamori JR**, Henderson BEP, et al. Single-cell transcriptomics uncovers zonation of function in the mesenchyme during liver fibrosis. Cell Rep 2019;29:1832–1847 e1838.
[2] Terkelsen MK, Bendixen SM, Hansen D, et al. Transcriptional dynamics of hepatic sinusoid-associated cells after liver injury. Hepatology 2020;72:2119–2133.
[3] **Xiong X**, **Kuang H**, **Ansari S**, et al. Landscape of intercellular crosstalk in healthy and NASH liver revealed by single-cell secretome gene analysis. Mol Cell 2019;75:644–660 e645.
[4] **Atasoy D**, **Aponte Y**, Su HH, et al. A FLEX switch targets Channelrhodopsin-2 to multiple cell types for imaging and long-range circuit mapping. J Neurosci 2008;28:7025–7030.
[5] Akhmedov D, Mendoza-Rodriguez MG, Rajendran K, et al. Gs-DREADD knock-in mice for tissue-specific, temporal stimulation of cyclic AMP signaling. Mol Cell Biol 2017:37.
[6] Mederacke I, Hsu CC, Troeger JS, et al. Fate tracing reveals hepatic stellate cells as dominant contributors to liver fibrosis independent of its aetiology. Nat Commun 2013;4:2823.
[7] **Marcher AB**, **Bendixen SM**, Terkelsen MK, et al. Transcriptional regulation of hepatic stellate cell activation in NASH. Sci Rep 2019;9:2324.
[8] **Clifford BL**, **Sedgeman LR**, Williams KJ, et al. FXR activation protects against NAFLD via bile-acid-dependent reductions in lipid absorption. Cell Metab 2021;33:1671–1684 e1674.
[9] Batth TS, Tollenaere MX, Ruther P, et al. Protein aggregation capture on microparticles enables multipurpose proteomics sample preparation. Mol Cell Proteomics 2019;18:1027–1035.
[10] Zhang B, Horvath S. A general framework for weighted gene co-expression network analysis. Stat Appl Genet Mol Biol 2005;4:Article17.
[11] Dann E, Henderson NC, Teichmann SA, et al. Differential abundance testing on single-cell data using k-nearest neighbor graphs. Nat Biotechnol 2022;40:245–253.
[12] Aibar S, Gonzalez-Blas CB, Moerman T, et al. SCENIC: single-cell regulatory network inference and clustering. Nat Methods 2017;14:1083–1086.
[13] Kalinichenko VV, Bhattacharyya D, Zhou Y, et al. Foxf1 +/- mice exhibit defective stellate cell activation and abnormal liver regeneration following CCl4 injury. Hepatology 2003;37:107–117.
[14] Wandzioch E, Kolterud A, Jacobsson M, et al. Lhx2-/- mice develop liver fibrosis. Proc Natl Acad Sci USA 2004;101:16549–16554.
[15] Schwabe RF, Tabas I, Pajvani UB. Mechanisms of fibrosis development in nonalcoholic steatohepatitis. Gastroenterology 2020;158:1913–1928.
[16] Remmerie A, Martens L, Thone T, et al. Osteopontin expression identifies a subset of recruited macrophages distinct from Kupffer cells in the fatty liver. Immunity 2020;53:641–657 e614.
[17] Seidman JS, Troutman TD, Sakai M, et al. Niche-specific reprogramming of epigenetic landscapes drives myeloid cell diversity in nonalcoholic steatohepatitis. Immunity 2020;52:1057–1074 e1057.
[18] **Tran S**, **Baba I**, Poupel L, et al. Impaired Kupffer cell self-renewal alters the liver response to lipid overload during non-alcoholic steatohepatitis. Immunity 2020;53:627–640 e625.
[19] **Peiseler M**, **Araujo David B**, Zindel J, et al. Kupffer cell-like syncytia replenish resident macrophage function in the fibrotic liver. Science 2023;381:eabq5202.
[20] Daemen S, Gainullina A, Kalugotla G, et al. Dynamic shifts in the composition of resident and recruited macrophages influence tissue remodeling in NASH. Cell Rep 2021;34:108626.
[21] Bergen V, Lange M, Peidli S, et al. Generalizing RNA velocity to transient cell states through dynamical modeling. Nat Biotechnol 2020;38:1408–1414.
[22] Sierro F, Evrard M, Rizzetto S, et al. A liver capsular network of monocyte-derived macrophages restricts hepatic dissemination of intraperitoneal bacteria by neutrophil recruitment. Immunity 2017;47:374–388 e376.
[23] **Scott CL**, **T'Jonck W**, Martens L, et al. The transcription factor ZEB2 is required to maintain the tissue-specific identities of macrophages. Immunity 2018;49:312–325 e315.
[24] **Bonnardel J**, **T'Jonck W**, Gaublomme D, et al. Stellate cells, hepatocytes, and endothelial cells imprint the Kupffer cell identity on monocytes colonizing the liver macrophage niche. Immunity 2019;51:638–654 e639.
[25] Desroches-Castan A, Tillet E, Ricard N, et al. Bone morphogenetic protein 9 is a paracrine factor controlling liver sinusoidal endothelial cell fenestration and protecting against hepatic fibrosis. Hepatology 2019;70:1392–1408.
[26] **Younossi ZM**, **Ratziu V**, Loomba R, et al. Obeticholic acid for the treatment of non-alcoholic steatohepatitis: interim analysis from a multicentre, randomised, placebo-controlled phase 3 trial. The Lancet 2019;394:2184–2196.
[27] **Tolbol KS**, **Kristiansen MN**, Hansen HH, et al. Metabolic and hepatic effects of liraglutide, obeticholic acid and elafibranor in diet-induced obese mouse models of biopsy-confirmed nonalcoholic steatohepatitis. World J Gastroenterol 2018;24:179–194.
[28] Wang S, Li K, Pickholz E, et al. An autocrine signaling circuit in hepatic stellate cells underlies advanced fibrosis in nonalcoholic steatohepatitis. Sci Transl Med 2023;15:eadd3949.
[29] Zhou J, Cui S, He Q, et al. SUMOylation inhibitors synergize with FXR agonists in combating liver fibrosis. Nat Commun 2020;11:240.
[30] Ijssennagger N, Janssen AWF, Milona A, et al. Gene expression profiling in human precision cut liver slices in response to the FXR agonist obeticholic acid. J Hepatol 2016;64:1158–1166.
[31] Neuschwander-Tetri BA, Loomba R, Sanyal AJ, et al. Farnesoid X nuclear receptor ligand obeticholic acid for non-cirrhotic, non-alcoholic steatohepatitis (FLINT): a multicentre, randomised, placebo-controlled trial. Lancet 2015;385:956–965.
[32] Fiorucci S, Antonelli E, Rizzo G, et al. The nuclear receptor SHP mediates inhibition of hepatic stellate cells by FXR and protects against liver fibrosis. Gastroenterology 2004;127:1497–1512.
[33] Fickert P, Fuchsbichler A, Moustafa T, et al. Farnesoid X receptor critically determines the fibrotic response in mice but is expressed to a low extent in human hepatic stellate cells and periductal myofibroblasts. Am J Pathol 2009;175:2392–2405.
[34] Verbeke L, Farre R, Trebicka J, et al. Obeticholic acid, a farnesoid X receptor agonist, improves portal hypertension by two distinct pathways in cirrhotic rats. Hepatology 2014;59:2286–2298.
[35] Schwabl P, Hambruch E, Seeland BA, et al. The FXR agonist PX20606 ameliorates portal hypertension by targeting vascular remodelling and sinusoidal dysfunction. J Hepatol 2017;66:724–733.
[36] **Garrido A**, **Kim E**, Teijeiro A, et al. Histone acetylation of bile acid transporter genes plays a critical role in cirrhosis. J Hepatol 2022;76:850–861.
[37] **Iwaisako K**, **Jiang C**, Zhang M, et al. Origin of myofibroblasts in the fibrotic liver in mice. Proc Natl Acad Sci USA 2014;111:E3297–E3305.

[38] Lei L, Bruneau A, El Mourabit H, et al. Portal fibroblasts with mesenchymal stem cell features form a reservoir of proliferative myofibroblasts in liver fibrosis. Hepatology 2022;76:1360–1375.
[39] Ferrell JM, Pathak P, Boehme S, et al. Deficiency of both farnesoid X receptor and takeda G protein-coupled receptor 5 exacerbated liver fibrosis in mice. Hepatology 2019;70:955–970.
[40] Chignard N, Mergey M, Barbu V, et al. VPAC1 expression is regulated by FXR agonists in the human gallbladder epithelium. Hepatology 2005;42:549–557.
[41] Sisson TH, Christensen PJ, Muraki Y, et al. Phosphodiesterase 4 inhibition reduces lung fibrosis following targeted type II alveolar epithelial cell injury. Physiol Rep 2018;6:e13753.
[42] **Surinkaew S**, **Aflaki M**, Takawale A, et al. Exchange protein activated by cyclic-adenosine monophosphate (Epac) regulates atrial fibroblast function and controls cardiac remodelling. Cardiovasc Res 2019;115:94–106.
[43] Lin SL, Chen RH, Chen YM, et al. Pentoxifylline attenuates tubulointerstitial fibrosis by blocking Smad3/4-activated transcription and profibrogenic effects of connective tissue growth factor. J Am Soc Nephrol 2005;16:2702–2713.
[44] Vilhais-Neto GC, Maruhashi M, Smith KT, et al. Rere controls retinoic acid signalling and somite bilateral symmetry. Nature 2010;463:953–957.
[45] **Ceni E**, **Mello T**, Polvani S, et al. The orphan nuclear receptor COUP-TFII coordinates hypoxia-independent proangiogenic responses in hepatic stellate cells. J Hepatol 2017;66:754–764.
[46] Liu X, Xu J, Rosenthal S, et al. Identification of lineage-specific transcription factors that prevent activation of hepatic stellate cells and promote fibrosis resolution. Gastroenterology 2020;158:1728–1744 e1714.
[47] **Lai T**, **Jabaudon D**, Molyneaux BJ, et al. SOX5 controls the sequential generation of distinct corticofugal neuron subtypes. Neuron 2008;57:232–247.
[48] Smits P, Li P, Mandel J, et al. The transcription factors L-Sox5 and Sox6 are essential for cartilage formation. Dev Cell 2001;1:277–290.
[49] **Guilliams M**, **Bonnardel J**, **Haest B**, et al. Spatial proteogenomics reveals distinct and evolutionarily conserved hepatic macrophage niches. Cell 2022;185:379–396 e338.
[50] Filliol A, Saito Y, Nair A, et al. Opposing roles of hepatic stellate cell subpopulations in hepatocarcinogenesis. Nature 2022;610:356–365.